Published version Open Access in Geosphere https://doi.org/10.1130/GES02686.1

Early Oligocene record of an Iceberg Alley in the Weddell Sea from quartz sand microtextural analysis at ODP Site 696

Victoria Hojnacki[1] and Sandra Passchier[1]

[1]*Department of Earth and Environmental Studies, Montclair State University, 1 Normal Avenue, Montclair, New Jersey, 07043, USA*

ABSTRACT

The greenhouse to icehouse transition at the Eocene-Oligocene boundary (34 Ma) marks the appearance of continental scale glaciation in Antarctica. The material recovered from the Ocean Drilling Program Site 696 is the only record spanning this major climatic shift in the Weddell Sea region. Using Scanning Electron Microscopy, quartz microtextures on thirteen samples across the Eocene-Oligocene Transition were analyzed to understand the degree of glacial modification and the transportation history of the >150μm material. The quartz grains were visually grouped, characterized and interpreted by grain outline, relief and surface microtextures. Glacial textures are present throughout the entire interval (33.2-34.4 Ma) with the proportion of iceberg-rafted grains in each sample decreasing into the Early Oligocene (33.6 Ma) accompanied by an increase in the frequency of eolian and sea-ice rafted grains. Mass accumulation rates reveal that the flux of iceberg rafted debris increases and is coincident with the flux of eolian and sea-ice rafted grains following 33.6 Ma, suggesting a strong coupling between land ice development and high-latitude atmospheric processes. When compared with other Antarctic climate proxy data sets, the intensification of ice rafting at Site 696 occurs after ice-sheet inception in East Antarctica. The prominent influx of terrigenous material after 33.6 Ma points to strengthened glacial conditions and, accompanied by major changes in the

environment of the Weddell Sea region, supports the idea of a high-latitude role in climate perturbations, in agreement with interpretations of other global proxies.

INTRODUCTION

The transition from greenhouse to icehouse conditions on Earth occurred around 34 million years ago in an event known as the Eocene-Oligocene transition (EOT). Oxygen isotope records from benthic foraminifera in the Eastern Equatorial Pacific reveal a two-step process across the EOT (Coxall et al., 2005; Coxall and Wilson, 2011). The initial step is attributed to cooling with a small increase in ice volume, while the second step of the oxygen isotope record is associated with a large ice volume increase (Lear et al., 2008). The second ice build-up is referred to as Oi-1 and represents the inception of a permanent ice sheet in Antarctica. The large response of the cryosphere at the EOT and the global transition to a different climate state is inferred to result from a climate overshoot, where the climate system surpasses the equilibrium state to an extreme and then returns to a more stable state, involving high-latitude atmospheric and ocean circulation feedbacks (Zachos and Kump, 2005).

Here we investigate the Antarctic record of the ice-sheet's inception and its high-latitude environmental impacts in the Weddell Sea. We use a systematic characterization of microtextures on quartz grain surfaces to track the glacial, marine and atmospheric transport history of sediment in a single drill hole spanning the EOT. Numerous studies confirm the existence of the East Antarctic Ice Sheet at the EOT (Scher et al., 2011; Passchier at al., 2017; Carter et al., 2017; Gulick et al., 2017). However, paleorecords provide varying time frames for the development of a marine-based West Antarctic Ice Sheet (Carter et al., 2017; Galeotti et al., 2016; Anderson et al., 2011). Previous grain texture work carried out on samples from Ocean Drilling Program (ODP) Hole 696B has provided evidence for ice rafting in the Weddell Sea almost 2.5 million years before the EOT (Carter et al., 2017). Additionally, upper Eocene sediments from the SHALDRIL expeditions in the Antarctic Peninsula region also contain ice-rafted debris with quartz grains exhibiting high angularity and glacial surface features. These textures are interpreted to represent early Alpine glaciation (Kirshner and Anderson, 2011), with large-scale West Antarctic Ice Sheet growth and expansion occurring in the Miocene (Anderson et al., 2011).

This study builds upon previous work by contributing a record of ice-rafted fluxes covering the Eocene-Oligocene transition. Microtextural analysis of quartz grains present an opportunity to understand the transportation history of coarse material in high-latitude marine mudstones (Helland and Holmes, 1997; St. John et al., 2015). Scanning electron microscopy (SEM) and a known group of surface textures can be used to identify past glacial transport (Whalley & Krinsley, 1974; Mahaney, 2002: Sweet & Brannan, 2016). Observations of iceberg-rafted debris (IBRD) released from icebergs calved from floating glacial ice, are separated from sea ice-rafted debris (SIRD) released from ice forming at the surface of the ocean during winter freezing. Distinguishing between these two types of ice rafting in environmental reconstructions is important because of the different roles of glacial ice vs. sea ice in Earth System processes. As the second step of the oxygen isotope record across the EOT is interpreted as a large ice volume increase (Lear et al., 2008), it is expected that quartz surface textures show an increase in glacial signature, i.e. IBRD, into the Early Oligocene due to glacial advance to the coast and increased iceberg rafting.

MATERIALS AND METHODS

The samples selected for analysis are from ODP Site 696. Hole 696B was drilled as a part of Leg 113 of the Ocean Drilling Program. Site 696, within Iceberg Alley, is located on the southeast margin of the South Orkney Microcontinent (61°50.959'S, 42°55.996'W) at a water depth of 650 meters (Figure 1). Icebergs calving off the Antarctic Ice Sheet follow the Antarctic Coastal Current into the Weddell Sea, where they melt and release sediment to the ocean floor, here tracked as IBRD. Therefore, this site provides the opportunity to obtain a record of ice sheet development.

Samples in this study are from subunit VIIB at 548.9-579.4 meters below seafloor (mbsf) and sample positions range in depth from 549.11 to 577.95 mbsf (Cores 696B-53R to 56R). The major lithology of the subunit is dark gray to black claystone and clayey mudstone. Within the subunit, small dropstones are reported in Cores 53R and 54R (Shipboard Scientific Party, 1988). Grain size distributions throughout subunit VIIB (Light, 2017; Lepp, 2018; Horowitz, 2021) were used, in addition to gravel occurrence (Shipboard Scientific Party, 1988), to select samples for this study. Thirty-three samples were disaggregated with deionized water and the use of an ultrasonic bath, before sieving to obtain the >150 µm fraction.

Thirteen samples with sufficient >150 µm weight percent were selected for further analysis using SEM. The >150 µm fraction of each of the 13 samples was viewed under an optical microscope and ~40 quartz grains were selected and mounted onto an aluminum stage with carbon tape. The grain mounts received a gold coating to reduce charging. Using a Hitachi S-3400N SEM in the Microscopy and Microanalysis Research Laboratory at Montclair State University, the grains were analyzed with a probe current of 50 mA and an accelerating voltage of 15 kV. Energy dispersive spectrometry (EDS) was used to verify the composition of each grain. Images of each grain were captured using a secondary electron (SE) detector. Grains that were not silica or those that had non-detrital morphology were excluded from further microtextural analysis. Inspection of the EDS signatures and SE images revealed a majority of the excluded grains were plagioclase or silicified remnants of foraminifera, diatoms, or radiolaria.

Prior to the detailed microtextural classification of the detrital quartz grains, the images of the quartz grains were randomly renamed to conceal their stratigraphic position in order to avoid bias in the identification of textures and depositional environments. The grains were visually classified into five grain types based on the environmental interpretation of the overall appearance of the grain (Hodel et al., 1988; Mahaney, 2002; Vos et al., 2014). The grains were then inspected with the use of a checklist including grain outline, grain relief, and 22 microtextures (Figure 2, Table 1). The textures encountered on a given grain were rated by the percent of grain coverage (absent <2%, present 2-25%, common 25-75%, abundant >75%). The results were analyzed by frequency of occurrence (%), defined by the percentage of grains with a given texture or of a given grain type in each sample.

According to the initial report from Site 696, material from subunit VIIB was tentatively thought to range in age from Early Miocene to Late Paleogene. Since the drilling of this site, dinocyst biostratigraphy was added to create an updated age model (Wei and Wise, 1990; Houben et al., 2011, 2013) that better constrains the EOT in Hole 696B. This study used the youngest four tie points from the age model developed by Hojnacki et al. (2022), based on datums in Houben et al. (2013). The linear sedimentation rate in the Late Eocene was ~ 2.2 cm/kyr. Sedimentation rate around the EOT slowed to ~ 0.5 cm/kyr, with a higher sedimentation rate of ~ 5.0 cm/kyr during the Early Oligocene.

Mass accumulation rates (MAR) were calculated using >150 µm weight fraction of the terrigenous material and values reported in the ODP Site 696 initial report. The following equations were used to calculate mass accumulation rates (St. John et al., 2008).

MAR = TERR CS x DBD x LSR (1)

Grain type MAR = TERR CS x DBD x LSR x grain type (2)

Where CS is the weight fraction of the >150 µm terrigenous material (Table S1), DBD is dry bulk density (Table S2), LSR is the linear sedimentation rate, and grain type is the frequency of the given grain type in the sample.

RESULTS

Grain Types

Grain types A through E are classified on the basis of grain outline, relief and the combination of microtextures present (Table 2; Figure 2). Textures are identified with the aid of observations and classification of grains from modern sedimentary environments (Mahaney, 2002; Vos et al., 2014). **Grain type A** is dominated by angular to subangular outlines and high stress textures like large conchoidal fractures, subparallel linear fractures, straight steps and fracture faces. These textures are common and occur on 50% or greater of type A grains. Grain type A ranges in frequency from 4 to 60% and is dominant in samples below ~569 mbsf, followed by a decline in frequency up core (Figure 3). **Grain type B** is dominated by subangular to subrounded outlines and dissolution weathering. Dissolution weathering is present on all grains within type B and generally covers more than 25% of the grain's surface. Type B grains range in frequency from 17 to 56%, with a general increase up core (Figure 3). **Grain type C** is subangular to subrounded in outline and contains abundant upturned plates. Upturned plates occur on over 90% of type C grains and a majority of those grains have upturned plates coverage greater than 25%. Type C grains range in frequency from 0 to 39%, with the highest frequencies occurring above ~ 563 mbsf (Figure 3). **Grain type D** is identified by euhedral overgrowth. Type D is only present in 4 of the 13 samples and makes up a small percentage of those samples

(Figure 3). **Grain type E** is composed of grains with subangular to subrounded outline with textures like conchoidal fractures, subparallel linear fractures, arcuate steps and V-shaped pits in low abundance (>40%). The frequency of type E grains ranges from 4 to 32% with a noticeable increase above ~563 mbsf (Figure 3). **Grain type F** is comprised of silica grains that are not terrigenous, and only make up 6 out of 378 total studied grains.

Stratigraphic changes in grain morphology, sand weight percent and IBRD MAR

Core 53R (548.9-558.5 mbsf): Four samples from Core 53R were analyzed for this study. The most abundant grain types in these samples are type B (34%) and type C (30%). Samples from core 53R are characterized by a subangular to subrounded outline. Adhering particles, dissolution weathering, and upturned plates are the most commonly occurring surface features with moderate frequency (Figure 4). Mechanical textures like large conchoidal fractures and subparallel linear fractures occur in lower frequencies. The samples in this core more commonly have chemical textures in comparison to mechanical. The dominance of chemical textures in this core is associated with a high proportion of type B grains.

Core 54R (558.5-568.2 mbsf): Three samples from Core 54R were analyzed. Core 54R grains are predominately type B (38%) and type C (33%). Samples from Core 54R are characterized by subangular to subrounded outline. Dissolution weathering, adhering particles, and upturned plates occur with moderate frequency (Figure 4). Low frequencies of large conchoidal fractures, subparallel linear fractures, straight and arcuate steps and fracture faces are noted. The high percentage of grain type B accounts for the high percentage of chemical features like dissolution weathering that is common in this core.

Core 55R (568.2-577.9 mbsf): Five samples from Core 55R were examined for surface textures. 50% of grains from Core 55R are classified as grain type A. These samples are characterized by a subangular to angular outline. Adhering particles and granular precipitation occur with high frequency in these samples (Figure 4). Mechanical textures such as large conchoidal fractures, subparallel linear fractures, straight and arcuate steps and fracture faces occur with moderate frequency.

Core 56R (577.9-587.6 mbsf): Only one sample was analyzed from Core 56R. Grain type A dominates the sample in this core accounting for 50%. This sample contains grains with subangular to angular outlines. Adhering particles and granular precipitation occur in high frequency (Figure 4). Mechanical features like large conchoidal fractures, subparallel linear fractures, straight and arcuate steps and fracture faces have moderate occurrences.

Microtextures commonly associated with glacial transport like large conchoidal fracture (>10μm), subparallel linear fracture, straight steps, arcuate steps, fracture face, straight groove, curved groove, and adhering particles (Whalley & Krinsley, 1974; Mahaney, 2002, Vos et al., 2014) generally show decreasing frequency up core (Figure 5). Similarly, grain outline decreases in angularity up core (Figure 6). The decrease in glacial textures and grain angularity occur while grain types B, C and E increase in frequency (Figure 3). Conversely, both >150 μm fraction weight percent and MAR increases above ~563 mbsf, with two peaks occurring at ~563 mbsf and ~552 mbsf (Figure 7).

DISCUSSION

Interpretation of Grain Types

Grains of **type A** are characterized by angular to subangular outline and high stress textures like large conchoidal fractures, subparallel linear fractures, straight steps and fracture faces, which are interpreted to represent iceberg rafted debris (IBRD) of primary glacial origin (Table 2) (Whalley & Krinsley, 1974; Mahaney, 2002; Vos et al., 2014). There is a relative difference, in degree of grain relief and crushing textures, between ice-sheet and alpine glacial quartz microtextures, however, the lack of secondary textures on type A grains support the interpretation of ice-sheet quartz microtextures (Mahaney et al., 1988). Grain **type B** exhibits common sea ice-rafted debris (SIRD) textures such as subrounded outlines and dissolution weathering (Dunhill, 1998; St. John et al., 2015). The difference in the grain morphology of iceberg and sea-ice rafted grains is caused by sea ice-rafted grains spending time in a periglacial environment and experiencing an overprinting of textures, while iceberg transport preserves the primary glacial signature characteristic of IBRD grains (St. John et al., 2015). Grain **type C** is dominated by upturned plates which is associated with eolian transport (Margolis & Krinsley, 1971; Vos et al., 2014; Mahaney, 2002). Grain **type E** is composed of grains with subangular to subrounded outline with textures like conchoidal fractures, subparallel linear fractures, arcuate steps and V-shaped impact pits in low frequencies. These grains have abraded surfaces and edge rounding and generally appear more mature than fresh glacial grains. The rounding and abrasion on these grains point to a low to moderate subaqueous transport (Hodel et al.,1988). Both Hodel et al. (1988) and Sweet and Brannan (2016) show that increased distance traveled downstream can cause the rounding and abrasion seen in type E grains.

Intensification of Ice Rafting

The results of this research indicate that quartz sand grains carrying a glacial signature are reaching Site 696 across the EOT. Iceberg rafted debris (IBRD) is present throughout the study interval in varying percentages. Previous work at Site 696 already provided evidence for iceberg-rafted and sea ice-rafted debris indicating glacial calving in the Weddell Sea region 2.5 million years prior to the EOT (Carter et al., 2017). However, microtextural work on SHALDRIL expedition samples indicates alpine glaciation of the Antarctic Peninsula occurred during the Late Eocene (Kirshner & Anderson, 2011). With the inclusion of previously unsampled cores spanning the EOT and the calculation of mass accumulation rates of iceberg-rafted debris (IBRD MAR), the record provides evidence for increasing glacial sediment supply after 33.6 Ma (Figure 7) while also supporting the findings of Carter et al (2017). The low occurrence of V-shaped percussions and edge rounding present on type A grains and the abundance of fresh glacial textures exclude the possibility the increased sedimentation rates of coarse fraction around ~33.6 Ma is related to bottom currents. As demonstrated by the work of Sweet and Brannan (2016), glacial textures decrease with the distance of bedload transport from a glacial source and fluvial (subaqueous transport) textures increase. Additionally, the increase in IBRD MAR coincides with the appearance of dropstones in the Early Oligocene (cores 53R and 54R). The heavy mineral assemblage of the >150 µm fraction points to a provenance in the sedimentary and metamorphic rocks of the southern and western Weddell Sea (Figure S2) for the IBRD MAR maxima in Cores 54R and 53R (above 563 mbsf; ~33.6 Ma) (Supplemental Material). The IRBD MAR and heavy mineral provenance indicates growth of the West Antarctic Ice Sheet in the Early Oligocene following East Antarctic ice advance, in agreement with the interpretation of the mud provenance for this site (Hojnacki et al., 2022).

Environmental Conditions in the Weddell Sea

The upcore decrease in the proportion of grains with glacial textures seen in the samples from Site 696 (Figure 4) is produced by an influx of grain types other than IBRD. The frequency of sea ice-rafted debris (SIRD), eolian, and periglacial grains increases after ~33.6 Ma (Figure 7). SIRD is present in moderate frequencies throughout the entire Eocene-Oligocene section but generally increases in the Oligocene (Figure 3). Increases in sea-ice formation during the expansion of the West Antarctic Ice Sheet explains the increased frequency and SIRD MAR throughout the study interval. The endemic Southern Ocean plankton ecosystem developed ~33.6 Ma and was driven by cooling and ice sheet expansion and associated sea-ice formation (Houben et al., 2013). The frequency of Protoperidiniaceae at Site 696 increases through the interval of this study. In particular, the appearance of *Selenopemphix antarctica*, coincides with the major peak of SIRD at 33.5 Ma (Figure 7) (Houben et al., 2013). *Selenopemphix antarctica* is a dominant dinocyst in the modern Antarctic sea-ice zone (Houben et al., 2013) and its abundance correlates with that of grain type B representing the seaice-rafted material.

In addition to the increase in ice-rafted material, eolian grains have a maximum abundance after 33.6 Ma. The increase in wind delivered grains to the site is coincident with glacial intensification and is consistent with the modeling efforts of Goldner et al (2014). The coupled ocean-atmosphere model demonstrates the effects of the inception of the Antarctic ice sheet. One of these effects includes changes in atmospheric circulation associated with the glacial topography of the continent, which increased surface wind around Antarctica (Goldner et al., 2014). There are multiple mechanisms through which these eolian grains could have been deposited. The deposition of the grains could be the result of deposition in water after wind transportation, transportation via sea-ice or via melting of ice shelves. Eolian sediments become concentrated in melt ponds on the top of ice shelves and during the break-up of an ice shelf, large amounts of these eolian deposits can be released to the sea floor (Gilbert and Domack, 2003). The low abundance of type E grains compared to the grain types A-D in the EOT sediment of Site 696, suggest that periglacial subaqueous modification of sand grains contributed less material than the primary IBRD, SIRD, and eolian fractions (Figure 7).

Geochemical and sedimentological data from around the Antarctic point to major changes in ice extent, glacial erosion, and high-latitude climate at the EOT (Figure 7). An oxygen isotope record from Maud Rise in the Southern Ocean shows a cooling and ice building phase associated with the greenhouse to icehouse transition (Diester-Haass & Zahn, 1996; Vonhof et al., 2000; Bohaty et al., 2012). Additionally, seawater neodymium isotopes from the Kerguelen Plateau in the Southern Ocean clearly demonstrate increased physical erosion signals associated with the expansion of the East Antarctic Ice Sheet followed by erosion repression due to a reduction in uncovered areas and a colder glacial regime (Scher et al., 2011). An upper Eocene diatomaceous claystone with interbedded sand in Prydz Bay is inferred as the arrival of glaciers at sea level (Strand et al., 2003). IBRD MAR from Site 696 in the Weddell Sea region of West Antarctica point to glacial intensification occurring in the Early Oligocene, later than the glacial expansion in East Antarctica (Figure 7) and increases in SIRD and eolian MARs confirm the results of previous studies (Houben et al., 2013; Goldner et al., 2014).

This study's record shows a peak pulse of >150 µm material followed by a return to background input (Figure 7) at the end of the EOT. This work and other global records document the climate system surpassing the equilibrium state (climate overshoot), ultimately returning to a more stable state. δ^{18}O values confirm a pattern of an abrupt positive shift at 33.7 Ma (Oi-1); following this event oxygen isotope values gradually begin to fall after 33 Ma (Diester-Haass and Zahn, 1996; Zachos et al., 1996; Coxall et al., 2011). Similar to the Site 696 record, IBRD deposition at the Kerguelen Plateau has a short episode (~75 kyr) of significant ice rafting at Oi-1 followed by a cessation of IBRD deposition (Scher et al., 2011). Along with the neodymium record, the Kerguelen Plateau IBRD record provides support to Zachos and Kumps (2005) modeling that suggests that the Oi-1 event is a climate overshoot and that the climate system eventually returned to a steady state after an increase in atmospheric CO_2 following a reduction in temperature and weatherable area. Site 696's peak in IBRD flux in the Early Oligocene signals marine ice-sheet growth, with IBRD delivery from the West Antarctic Ice Sheet, followed by a return to a more reduced stable ice sheet, and a reduction in the IBRD flux into the Weddell Sea. Site 696, located within the modern-day Iceberg Alley, allowed for the observation of this climate overshoot at a high-latitude site in the Weddell Sea.

CONCLUSIONS

A transportation history of sand grains within Iceberg Alley in the Weddell Sea region during the EOT is provided by microtextural analysis of samples from ODP Site 696. The presence of grains exhibiting typical glacial textures in all samples confirm that icebergs are reaching the region from the Late Eocene to the Early Oligocene. Mass accumulation rates of the IBRD and SIRD fraction provide evidence for intensification of glacial conditions around 33.6 Ma, after the growth and expansion of the East Antarctic Ice Sheet. The increase in glacial grains is accompanied by an influx of eolian grains demonstrating the changing surface climate conditions associated with the development of the Antarctic Ice Sheet. The pulse of >150 µm material at the site at 33.5 Ma supports the idea of ice-sheet overshoot in the Early Oligocene.

ACKNOWLEDGEMENTS

This research used samples and/or data provided by the Ocean Drilling Program (ODP). This project was supported by NSF Award 1743643 to SP. Dr. Laying Wu (Microscopy and Microanalysis Research Laboratory at Montclair State University) is thanked for her guidance with sample preparation for the SEM work. We thank three anonymous reviewers for their suggestions and insights.

REFERENCES CITED

Anderson, J.B., Warny, S., Askin, R.A., Wellner, J.S., Bohaty, S.M., Kirshner, A.E., Livsey, D.N., Simms, A.R., Smith, T.R., Ehrmann, W. & Lawver, L.A., 2011, Progressive Cenozoic cooling and the demise of Antarctica's last refugium: Proceedings of the National Academy of Sciences of the United States of America, v. 108, p. 11356–11360, doi:10.1073/pnas.1014885108.

Bohaty, S.M., Zachos, J.C., & Delaney, M.L., 2012, Foraminiferal Mg/Ca evidence for Southern Ocean cooling across the Eocene-Oligocene transition: Earth and Planetary Science Letters, v. 317-318, p. 251-261, doi:10.1016/j.epsl.2011.11.037.

Carter, A., Riley, T.R., Hillenbrand, C., & Rittner, M., 2017, Widespread Antarctic glaciation during the late Eocene: Earth and Planetary Science Letters, v. 458, p. 49–57, doi:10.1016/j.epsl.2016.10.045.

Coxall, H.K., & Wilson, P.A., 2011, Early Oligocene glaciation and productivity in the eastern equatorial Pacific: Insights into global carbon cycling: Paleoceanography and Paleoclimatology, v. 26, doi:10.1029/2010PA002021.

Coxall, H.K., Wilson, P.A., Pälike, H., Lear, C.H., & Backman, J., 2005, Rapid stepwise onset of Antarctic glaciation and deeper calcite compensation in the Pacific Ocean: Nature, v. 433, p. 53–57, doi: 10.1038/nature03135.

Diester-Haass, L. & Zahn,R., 1996, Eocene-Oligocene transition in the Southern Ocean: History of water mass circulation and biological productivity: Geology, v. 24, p. 163-166, doi:10.1130/0091-7613(1996)024<0163:EOTITS>2.3.CO;2.

Dunhill, G., 1998, Comparison of Sea-Ice and Glacial-Ice Rafted Debris Grain Size, Surface Features, and Grain Shape: USGS Open File Report 98-367.

Galeotti, S., et al., 2016, Antarctic Ice Sheet variability across the Eocene-Oligocene boundary climate transition: Science, v. 352, p. 76-80, doi:10.1126/science.aab0669.

Gilbert R., & Domack, E.W., 2003, Sedimentary record of disintegrating ice shelves in a warming climate, Antarctic Peninsula: Geochemistry, Geophysics, Geosystems, v4, no. 4, doi:10.1029/2002GC000441.

Goldner, A., Herold, N. & Huber, M., 2014, Antarctic glaciation caused ocean circulation changes at the Eocene-Oligocene transition: Nature, v. 511, p. 574-577, doi: 10.1038/nature13597.

Gulick, S.P.S, Shevenell, A.E., Montelli, A., Fernandez, R., Smith, C., Warny, S., Bohaty, S.M., Sjunneskog, C., Leventer, A., Frederick, B., & Blankenship, D.D., 2017, Initiation and long-term instability of the East Antarctic Ice Sheet: Nature, v 552, p. 225-229, doi.org/10.1038/nature25026

Helland, P.E. & Holmes, M.A., 1997, Surface textural analysis of quartz sand grains from ODP Site 918 off the southeast coast of Greenland suggest glaciation of southern Greenland at 11 Ma: Palaeogeography, Palaeoclimatology, Palaeoecology, v. 135, p. 109-121, doi:10.1016/S0031-0182(97)00025-4.

Hodel, K.L., Reimnitz, E., & Barnes, P.W., 1988, Microtextures of quartz grains from modern terrestrial and subaqueous environments, North Slope of Alaska: Journal of Sedimentary Petrology, v. 58, p. 24-32, doi:10.1306/212F8D00-2B24-11D7-8648000102C1865D.

Hojnacki, V., Lepp, A., Horowitz Castaldo, J., States, A., Li, X., & Passchier, S., 2022, Impact of Eocene-Oligocene Antarctic glaciation on the paleoceanography of the Weddell Sea: Paleoceanography and Paleoclimatology, v. 37, doi: 10.1029/2022PA004440

Horowitz, J., 2021, Identification of ice-rafted debris in the Weddell Sea to characterize glaciation at the Eocene-Oligocene transition [M.S. Thesis]: Montclair State University.

Houben, A. J., Bijl, P. K., Guerstein, G. R., Sluijs, A., & Brinkhuis, H., 2011, Malvinia escutiana, a new biostratigraphically important Oligocene dinoflagellate cyst from the Southern Ocean: Review of Palaeobotany and Palynology, v. 165(3-4), p. 175-182, doi:10.1016/j.revpalbo.2011.03.002.

Houben, A.J.P., et al., 2013, Reorganization of Southern Ocean plankton ecosystem at the onset of Antarctic glaciation: Science, v. 340, p. 341–344, doi:10.1126/science.1223646.

Kirshner, A. E., & Anderson, J. B., 2011, Cenozoic glacial history of the northern Antarctic Peninsula: A micromorphological investigation of quartz sand grains, in Anderson, J.B., and Wellner, J., eds., Tectonic, climatic, and cryospheric evolution of the Antarctic Peninsula, American Geophysical Union, v. 63, p. 153-165, doi:10.1029/SP063.

Lear, C.H., Bailey, T.R., Pearson, P.N., Coxall, H.K. & Rosenthal, Y., 2008, Cooling and ice growth across the Eocene-Oligocene transition: Geology, v. 36, p. 251–254, doi:10.1130/G24584A.1.

Lepp, A.P., 2018, Geochemical and sedimentological analysis of marine sediments from ODP Site 696 and implications for the onset of Antarctic glaciation [M.S. Thesis]: Montclair State University.

Light, J.J, 2017, Geochemical and particle size analysis of East Antarctic shelf sediments through the Eocene Oligocene transition [M.S. Thesis]: Montclair State University.

Mahaney, W.C., 2002, Atlas of Sand Grain Surface Textures and Applications: New York, Oxford University Press, 237 p.

Mahaney, W.C., Vortisch, W., & Julig, P., 1988, Relative differences between glacially crushed quartz transported by mountain and continental ice, some examples from North America and East Africa: American Journal of Science, v. 288, p. 810–826, doi:10. 2475/ajs.288.8.810

Margolis, S.V., & Krinsley, D.H., 1971, Submicroscopic frosting on eolian and subaqueous quartz sand grains: Geological Society of American Bulletin, v. 82, p. 3395-3406, doi:10.1130/0016-7606(1971)82[3395:SFOEAS]2.0.CO;2.

Passchier, S., Ciarletta, D.J., Miriagos, T.E., Bijl, P.K. & Bohaty, S.M., 2017, An Antarctic stratigraphic record of stepwise ice growth through the Eocene-Oligocene transition: Bulletin of the Geological Society of America, v. 129, p. 318–330, doi:10.1130/B31482.1.

Scher, H.D., Bohaty, S.M., Zacos, J.C. & Delaney, M.L., 2011,Two-stepping into the icehouse: East Antarctic weathering during progressive ice-sheet expansion at the Eocene–Oligocene transition: Geology, v. 39(4), 383–386, doi:10.1130/G31726.1.

Shipboard Scientific Party, 1988, Site 696, in Barker, P. F., Kennett, J. P., et al., Proceedings of the Ocean Drilling Program, Initial Reports, 113: College Station, TX.

St. John, K., 2008, Cenozoic ice-rafting history if the central Arctic Ocean: Terrigenous sands on the Lomonosov Ridge: Paleoceanography and Paleoclimatology , v. 23, doi: 10.1029/2007PA001483.

St. John, K., Passchier, S., Tantillo, B., Darby, D., & Kearns, L., 2015, Microfeatures of modern sea-ice-rafted sediment and implications for paleo-sea-ice reconstructions: Annals of Glaciology, v. 56, p. 83-93, doi:10.3189/2015AoG69A586.

Sweet, D.E., & Brannan, D.K., 2016, Proportion of glacially to fluvially induced quartz grain microtextures along the Chitina River, SE Alaska, U.S.A.: Journal of Sedimentary Research, v. 86, p. 749-761, doi:10.2110/jsr.2016.49.

Strand, K., Passchier, S., & Näsi, J., 2003, Implications of quartz grain microtextures for the onset Eocene/Oligocene glaciation in Prydz Bay, ODP Site 1166, Antarctica: Palaeogeography, Palaeoclimatology, Palaeoecology, v. 198, p. 101-111, doi:10.1016/S0031-0182(03)00396-1.

Vonhof, H.B., Smit, J., Brinkhuis, H., Montanari, A., & Nederbragt, A.J., 2000, Global cooling accelerated by early late Eocene impacts: Geology, v. 28, p. 687-690, doi:10.1130/0091-7613(2000)28<687:GCABEL>2.0.CO;2.

Vos, K., Vandenberghe, N., & Elsen, J., 2014, Surface textural analysis of quartz grains by scanning electron microscope (SEM): From sample preparation to environmental interpretation: Earth-Science Reviews, v. 128, p. 93-104, doi:10.1016/j.earscirev.2013.10.013

Whalley, B., & Krinsley, D., 1974, A scanning electron microscope study of surface textures of quartz grains from glacial environments: Sedimentology, v. 21, p. 87-105, doi:10.1111/j.1365-3091.1974.tb01783.x

Wei, W. & Wise, S.W., 1990, Middle Eocene to Pleistocene calcareous nannofossils recovered by Ocean Drilling Program Leg 113 in the Weddell Sea, in Barker, PF; Kennett, JP; et al., Proceedings of the Ocean Drilling Program, Scientific Results, College Station, TX, p. 639-666.

Zachos, J.C., & Kump, L.R., 2005, Carbon cycle feedbacks and the initiation of Antarctic glaciation in the earliest Oligocene: Global and Planetary Change, 47, p. 51-66, doi:10.1016/j.gloplacha.2005.01.001

Zachos, J. C., Quinn, T.M., & Salamy, K.A., 1996, High-resolution (104 years) deep-sea foraminiferal stable isotope records of the Eocene-Oligocene climate transition, Paleoceanography and Paleoclimatology, 11, p. 251–266, doi:10.1029/96PA00571

Figure and Table Captions

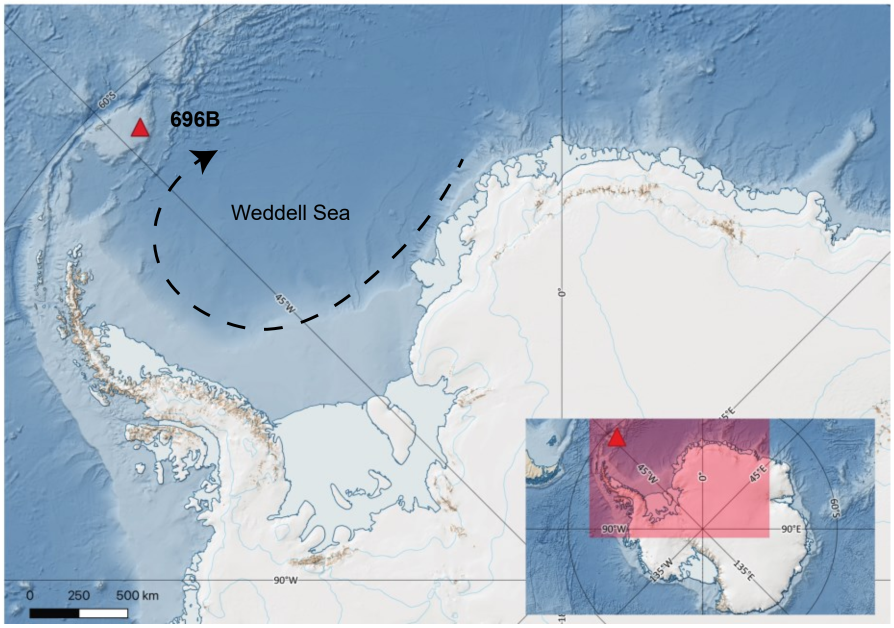

Figure 1. Map of Antarctica with a red triangle in the Weddell Sea representing ODP Site 696. The dashed black arrow denotes the path of icebergs in Iceberg Alley. Map produced using the Quantarctica compilation in QGIS.

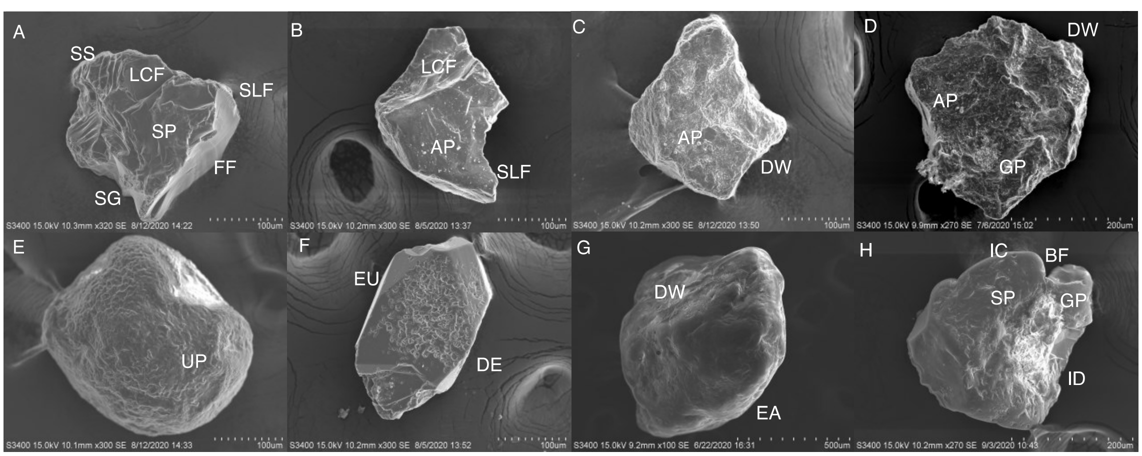

Figure 2. SEM micrographs of grains from ODP Site 696. (A) Grain type A with an angular outline, high relief, large concoidal fracture, subparallel linear fracture, straigh steps, fracture face, straight groove, and solution pits. (B) Grain type A with a subangular outline, medium relief, large conchoidal fracture, subparallel linear fracture and adhering particles. (C) Grain

type B with a subangular outline, medium relief, dissolution weathering and adhering particles. (D) Grain type B with subangular outline, medium relief, dissolution weathering, adhering particles and granular precipitation. (E) Grain type C with a subrounded outline, medium relief, and upturned plates. (F) Grain type D with an angular outline, low relief, euhedral overgrowth and dissolution etching. (G) Grain type E with a rounded outline, medium relief, dissolution weathering and edge abrasion. (H) Grain type E with a subrounded outline, medium relief, irregular dish-shaped depressions, impact crators, solution pits, granular precipitation and a bulbous feature. AP = adhering particles, DW = dissolution weathering, GP = granular precipitation, UP = upturned plates, EU = euhedral overgrowth, DE = dissolution etching, EA = edge abrassion, IC = impact crators, SP = solution pits, BF = bulbous feature, ID = irregular dish-shaped depression, SS = straight steps, LCF = large conchoidal fracture (>10 µm), SLF = subparallel linear fracture, FF = fracture face, SG = straight groove.

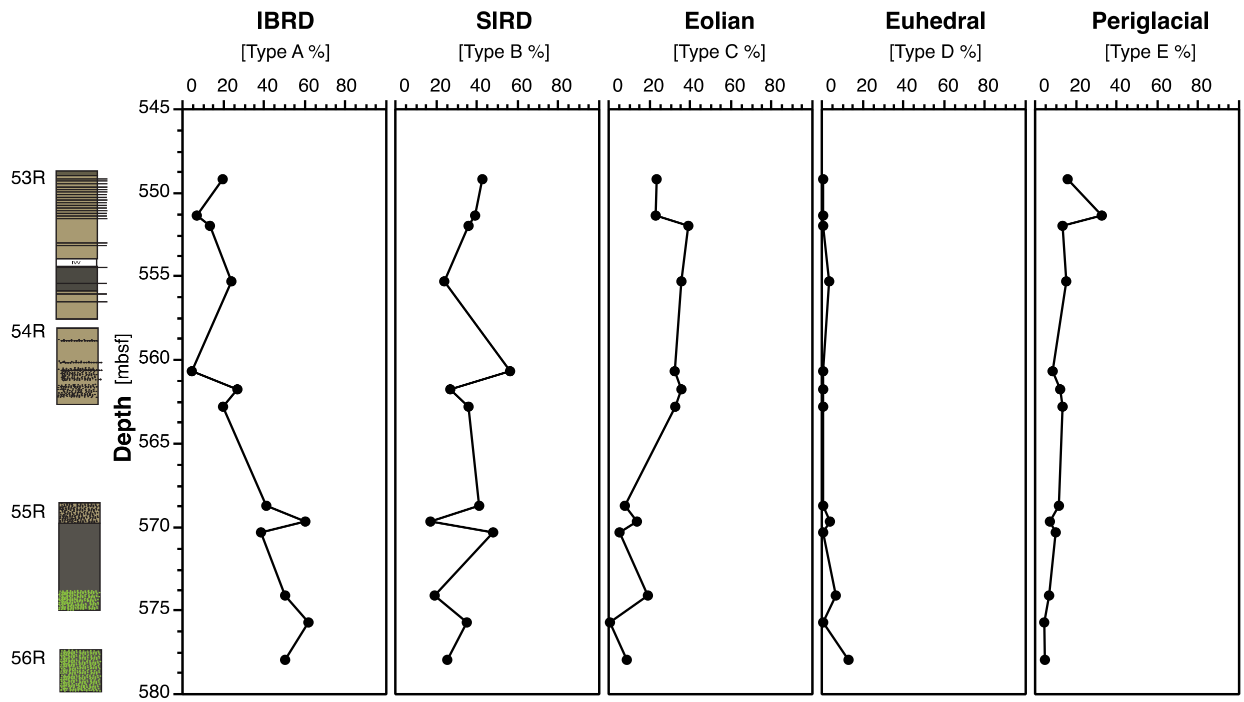

Figure 3: Lithologic log after Hojnacki at al. (2022). Grain type frequency (%) plots by depth. Grain types B, C and E increase up core, while type A decreases.

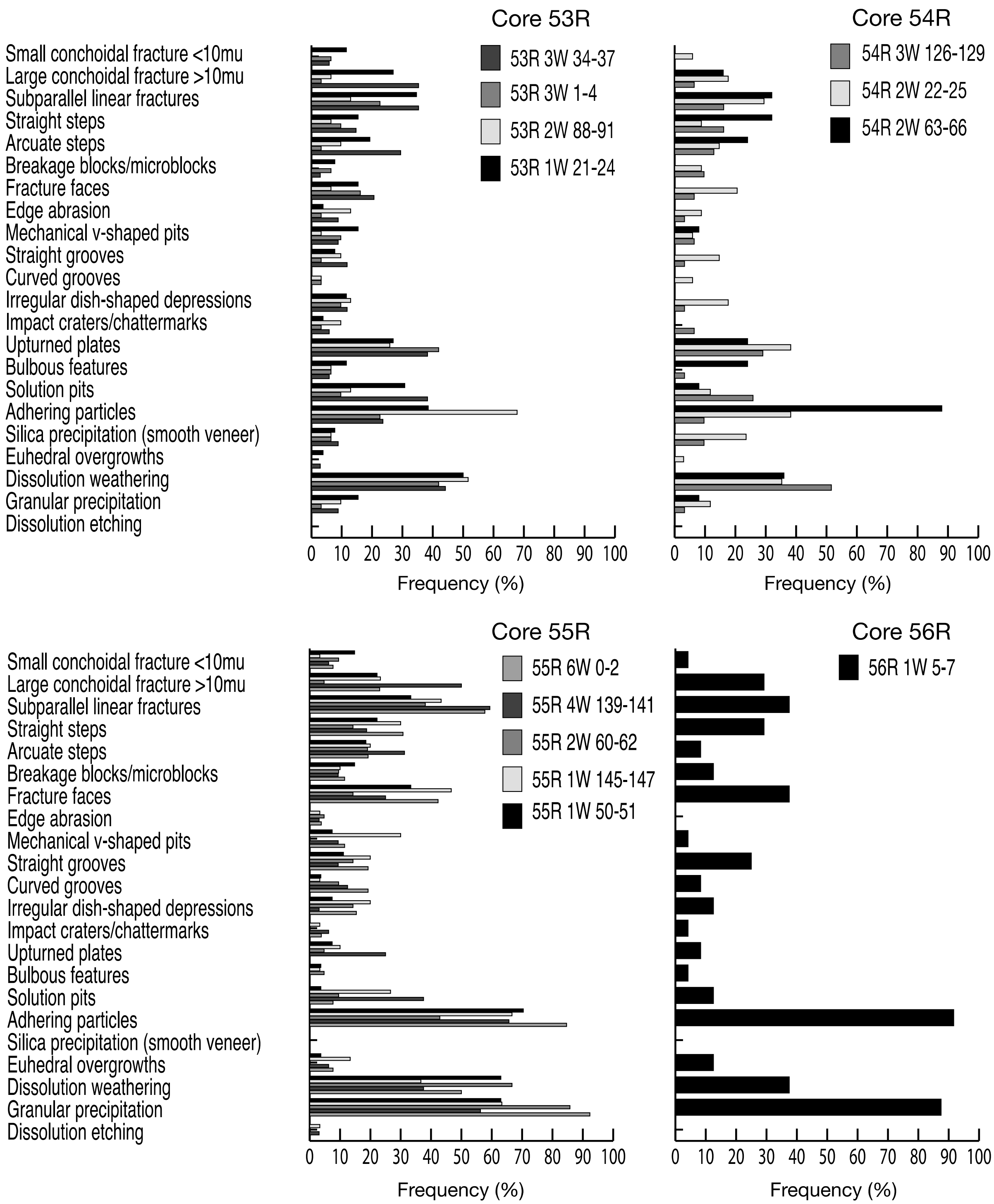

Figure 4. Frequency of occurrence (%), defined as percentage of grains exhibiting each surface texture in samples by core.

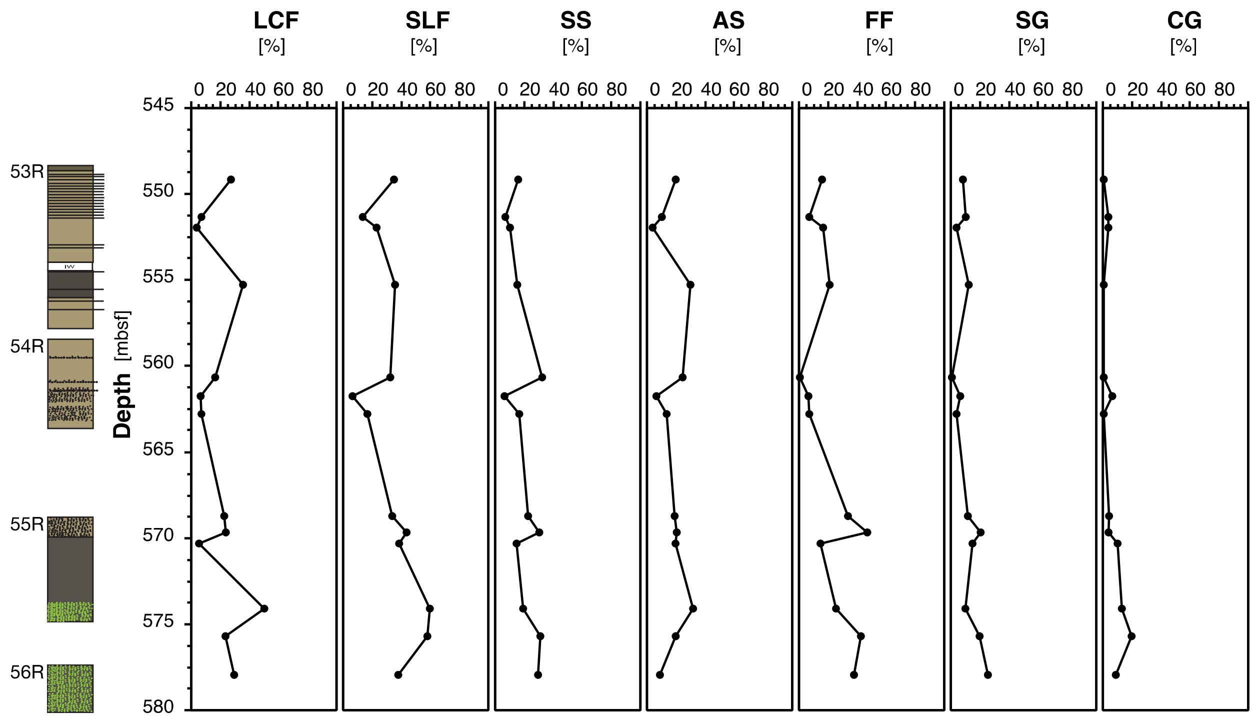

Figure 5. Changes in glacial texture frequency by depth. Glacial textures generally decrease up core. LCF = large conchoidal fracture >10µm, SLF = subparallel linear fracture, SS = straight steps, AS = arcuate steps, FF = fracture face, SG = straight groove, CG = curved groove, AP = adhering particle.

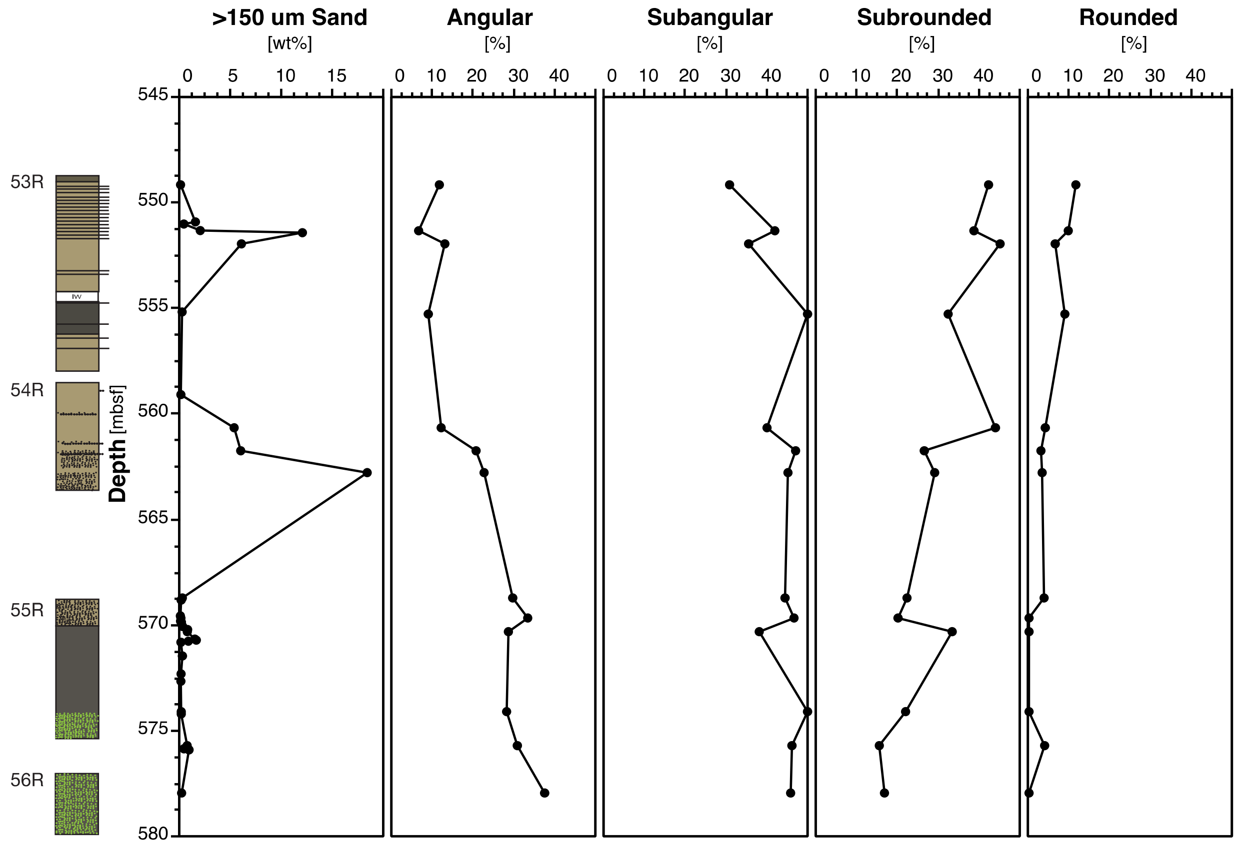

Figure 6. Changes in >150 um weight percent and grain outline frequency by depth. Angular outlines decrease up core, while rounded outlines increase.

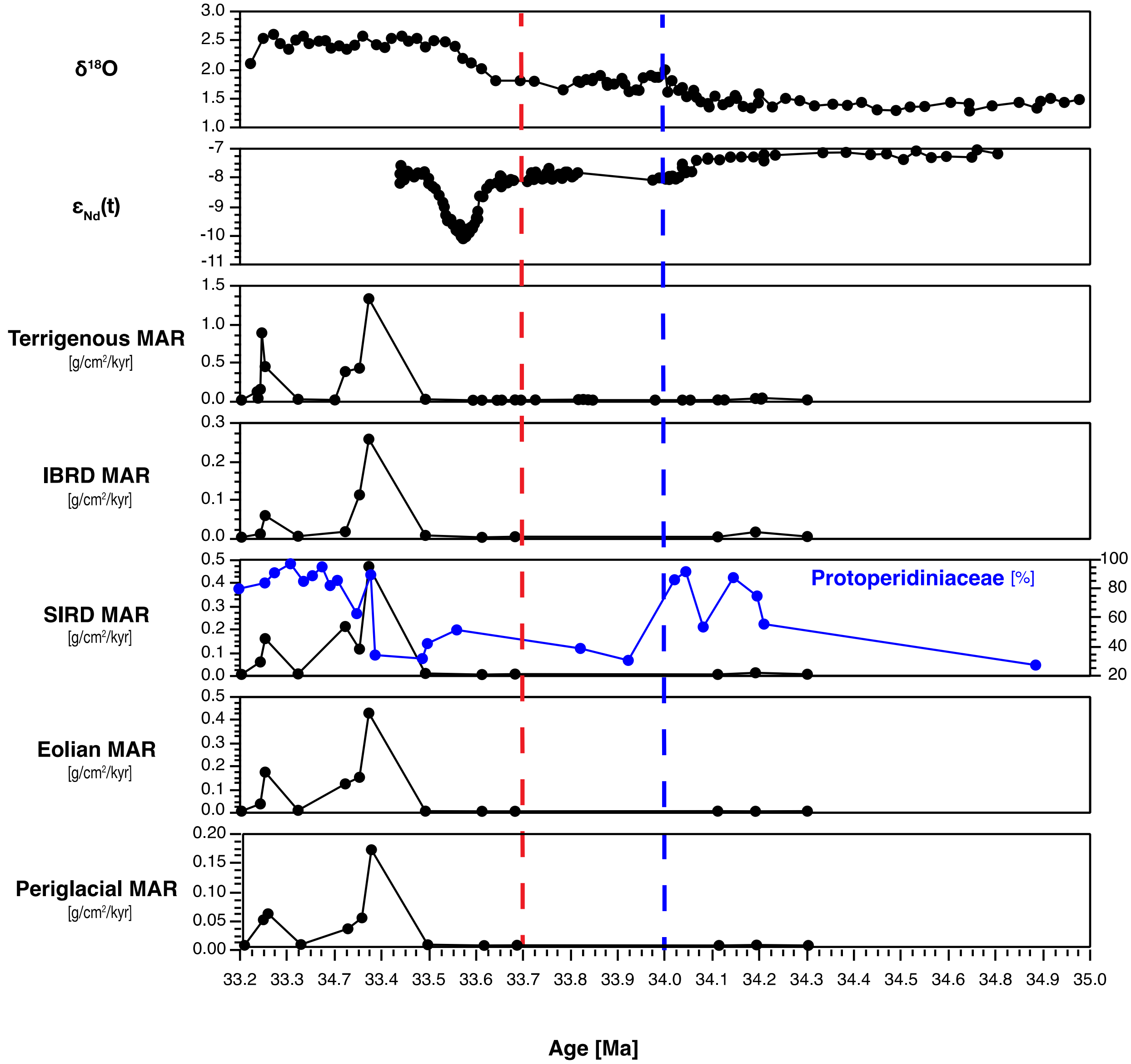

Figure 7 – Mass Accumulation rates of bulk terrigenous and iceberg (type A), sea-ice (Type B), eolian (Type C), and periglacial (Type E) grain types plots on an age model (GTS2012). All grain types exhibit a major change after ~33.6 Ma when the Antarctic Ice Sheet is expanding. Oxygen isotope data are from ODP site 689 at Maud Rise (Diester-Haass & Zahn, 1996; Vonhof et al., 2000; Bohaty et al., 2012), seawater neodymium isotope ratios are from Kerguelen Plateau (Scher et al., 2011), and protoperidiniaceae frequency is from site 696 (Houben et al., 2013). The EOT is marked by the blue line. Oi-1 is marked by the red line.

TABLE 1: FREQUENCY (%) OF SURFACE TEXTURES BY SAMPLE

Surface features	Sample ID												
	1	2	3	4	5	6	7	8	9	10	11	12	13
<u>Outline</u>													
Very angular	4	3	0	0	0	3	0	0	0	0	0	4	0
Angular	12	6	13	9	12	21	23	30	33	29	28	31	38
Sub-angular	31	42	35	50	40	47	45	44	47	38	50	46	46
Sub-rounded	42	39	45	32	44	26	29	22	20	33	22	15	17
Rounded	12	10	6	9	4	3	3	4	0	0	0	4	0
Well-rounded	0	0	0	0	0	0	0	0	0	0	0	0	0
<u>Relief</u>													
High	4	0	3	3	8	3	6	7	7	10	9	4	4
Medium	73	94	77	82	84	91	90	63	60	71	66	50	50
Low	23	6	19	15	8	6	3	30	33	19	25	46	46
<u>Mechanical Textures</u>													
Small conchoidal fracture <10mu	12	0	6	6	0	6	0	15	3	10	6	8	4
Large conchoidal fracture >10mu	27	6	3	35	16	18	6	22	23	5	50	23	29
Subparallel linear fractures	35	13	23	35	32	29	16	33	43	38	59	58	38
Straight steps	15	6	10	15	32	9	16	22	30	14	19	31	29
Arcuate steps	19	10	3	29	24	15	13	19	20	19	31	19	8
Breakage blocks/microblocks	8	0	6	3	0	9	10	15	10	10	9	12	13
Fracture faces	15	6	16	21	0	21	6	33	47	14	25	42	38
Edge abrasion	4	13	3	9	0	9	3	0	3	5	3	4	0
Mechanical v-shaped pits	15	3	10	9	8	6	6	7	30	0	9	12	4
Straight grooves	8	10	3	12	0	15	3	11	20	14	9	19	25
Curved grooves	0	3	3	0	0	6	0	4	3	10	13	19	8
Irregular dish-shaped depressions	12	13	10	12	0	18	3	7	20	14	3	15	13
Impact craters/chattermarks	4	10	3	6	0	0	6	0	3	0	6	4	4
Upturned plates	27	26	42	38	24	38	29	7	10	5	25	0	8
Bulbous features	12	6	6	6	24	0	3	4	3	5	0	0	4
<u>Chemical Textures</u>													
Solution pits	31	13	10	38	8	12	26	4	27	10	38	8	13
Adhering particles	38	68	23	24	88	38	10	70	67	43	66	85	92
Silica precipitation (smooth veneer)	8	6	6	9	0	24	10	0	0	0	0	0	0
Euhedral overgrowths	4	0	0	3	0	3	0	4	13	0	6	8	13
Dissolution weathering	50	52	42	44	36	35	52	63	37	67	38	50	38
Granular precipitation	15	10	3	9	8	12	3	63	63	86	56	92	88
Dissolution etching	0	0	0	0	0	0	0	0	3	0	3	0	0

Table 1. Frequency (%) of surface features by sample. Sample IDs: 1 = 53R 1W 21-24; 2 =53R 2W 88-91; 3 = 53R 3W 1-4; 4 = 53R 5W 34-37; 5 = 54R 2W 63-66; 6 = 54R 3W 22-25; 7 = 54R 3W 126-129; 8 = 55R 1W 50-51; 9 = 55R 1W 145-147; 10 = 55R 2W 60-62; 11 = 55R 4W 139-141; 12 = 55R 6W 0-2; 13 = 56R 1W 5-7.

TABLE 2. GRAIN TYPE SUMMARY

Grain type	Outline	Relief	Textures	Interpretation
A	Angular to Subangular	Varied	Large conchoidal fractures, subparallel linear fractures, straight steps and fracture faces	Iceberg rafted debris
B	Subangular to subrounded	Medium	Abundant dissolution weathering	Sea-ice rafted debris
C	Subangular to subrounded	Medium	Abundant upturned plates	Eolian transport
D	Angular to subangular	High to medium	Euhedral overgrowth	Chemical alternation
E	Subangular to subrounded	Medium	Conchoidal fractures, subparallel linear fractures, arcuate steps and V-shaped pits in low abundance	Periglacial

Table 2. Description and interpretation of grain types.